ChemComm

HIGHLIGHT

Cite this: *Chem. Commun.*, 2025, **61**, 10200

Recent advancements of bismuth titanate photocatalysis

Xiang Sui,[a] Runjie Wu,[a] Mingming Sun,[a] Ming Guo,[a] Zeping Qin,[a] Pengkun Li,[a] Xingrui Liu,[a] Davida Briana DuBois,[b] Shaowei Chen *[b] and Qiang Wang *[a]

Received 19th February 2025,
Accepted 10th June 2025

DOI: 10.1039/d5cc00928f

rsc.li/chemcomm

Bismuth titanate has found widespread applications in photocatalysis for hydrogen production, degradation of organic pollutants, nitrogen oxide removal, and carbon dioxide reduction, among others, due to its unique crystal structure and electronic energy band configuration. In this paper, we summarize the recent progress in the preparation of bismuth titanate, mainly $Bi_2Ti_2O_7$, which is classified into four categories according to their morphological and structural characteristics, explore the manipulation of the materials morphology, and analyze the influence of the materials structures on the photocatalytic performance. The review is concluded with a perspective highlighting the key challenges and future research directions.

1. Introduction

Photocatalysis has been widely used as an environmentally friendly technology for sustainable energy storage/conversion and environmental remediation, where rational design and engineering of effective photocatalysts represents a critical first step in dictating the photocatalytic performance.[1,2] Titanium dioxide (TiO_2) is a well-known photocatalyst by virtue of its apparent photocatalytic activity, high stability, and low cost. However, the large bandgap (*ca.* 3.2 eV) and low quantum yield greatly limit its application.[3,4] Recently, bismuth titanate has emerged as a viable option with its unique material morphology and electronic band structure.[2] In comparison to TiO_2, bismuth titanate exhibits a narrower bandgap (*ca.* 2.7–2.9 eV), which enables efficient utilization of visible light, and its ferroelectric properties can facilitate the separation of photogenerated electron–hole pairs, significantly enhancing the photocatalytic efficiency. Moreover, bismuth titanate demonstrates excellent chemical stability and environmental compatibility.[5] In fact, bismuth titanate has found diverse applications, such as photocatalytic degradation of organic pollutants,[6–8] hydrogen evolution,[9–11] removal of nitrogen oxides,[12–14] and carbon reduction,[15] among others.

Bismuth titanate exhibits various phase structures, such as $Bi_2Ti_2O_7$ (pyrochlore),[16] $Bi_{12}TiO_{20}$ (sillenite),[17] $Bi_{20}TiO_{32}$ (metastable phase),[18] $Bi_4Ti_3O_{12}$ (perovskite-like),[19] and $Bi_2Ti_4O_{11}$.[20] Among these, the pyrochlore-phase $Bi_2Ti_2O_7$ is the most widely utilized. It belongs to the $A_2B_2O_7$ compound family, characterized by A_2O tetrahedral frameworks sharing corners with BO_6 octahedra. This structure can also be represented as $A_2B_2O_6O'$. The high lattice disorder of $Bi_2Ti_2O_7$ increases the ion migration rate within the material, promoting the formation of abundant oxygen vacancies, thereby significantly enhancing the catalytic activity and stability.[21] Pyrochlore-phase $Bi_2Ti_2O_7$ is typically synthesized as very small nanoparticles. The Bi ions occupy the A sites, interact through the 6s and 6p orbitals, and cause simultaneous shifts of the valence band (VB) and conduction band (CB) of $Bi_2Ti_2O_7$, leading to enhanced electron mobility and photocatalytic activity.[22]

$Bi_2Ti_2O_7$ can be classified into four groups based on the material's morphology (Fig. 1): zero-dimensional (0D) nanoparticles/nanospheres,[16,23–26] one-dimensional (1D) nanotubes,[6] nanorods,[9] nanobelts,[5] and nanofibers,[27] two-dimensional (2D) nanoplates[19] and nanofilms,[28] and three-dimensional (3D) nanoflowers.[13] It is worth noting that the material morphology, specific surface area, crystal structure, photoelectric response, carrier transport rate, and oxygen vacancy concentration can all greatly impact the photocatalytic activity.[29–32] For instance, Krasnov *et al.*[33] conducted computational studies based on density functional theory (DFT) calculations of alkaline-earth element-doped pyrochlore bismuth titanate, and found that the alkaline-earth elements preferentially substituted the A sites of the pyrochlore structure and the doping transformed $Bi_2Ti_2O_7$ into a wide-bandgap semiconductor material. By controlling the doping concentration, the authors successfully obtained a new phase of pyrochlore, $Bi_{1.5}Ca_{0.25}Ti_2O_{7-\delta}$, with minimal impurities, where the activation energy within the temperature range of 200–750 °C was *ca.* 1.00 eV. Among these, Ca-doped $Bi_{1.5}Ca_{0.25}Ti_2O_{7-\delta}$

[a] *Laboratory for Micro-sized Functional Materials & College of Elementary, Education and Department of Chemistry, Capital Normal University, Beijing 100048, China. E-mail: qwchem@gmail.com*
[b] *Department of Chemistry and Biochemistry, University of California, 1156 High Street, Santa Cruz, CA95064, USA. E-mail: shaowei@ucsc.edu*

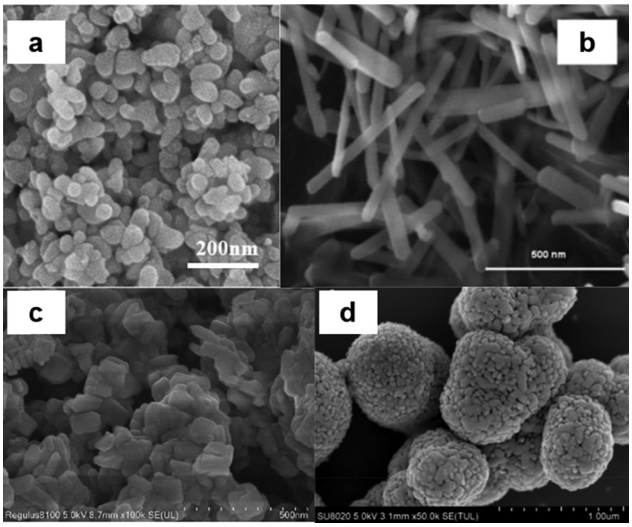

Fig. 1 (a) $Bi_2Ti_2O_7$ nanoparticles. Reproduced or adapted with permission from ref. 34. Copyright 2022 Elsevier. (b) $Bi_2Ti_2O_7$ nanorods. Reproduced or adapted with permission from ref. 35. Copyright 1996 Elsevier. (c) $Bi_2Ti_2O_7$ nanosheets. Reproduced or adapted with permission from ref. 36. Copyright 2023 Elsevier. (d) $Bi_2Ti_2O_7$ nanoflowers. Reproduced or adapted with permission from ref. 37. Copyright 2020 Elsevier.

was confirmed to be a mixed ion-electron conductor, with an indirect bandgap of *ca.* 2.3 eV and a direct bandgap of *ca.* 2.4 eV. The Ca 4s, 3p, and 3d orbitals contributed to the formation of the VB and partially to the CB.[33]

In this review, we will summarize the synthesis methods, analyze the materials morphologies and modification strategies, and highlight the state of the art of the photocatalytic applications of bismuth titanate. We will then discuss strategies for materials structural engineering and new applications. We conclude the review with a highlight of the remaining challenges and future research directions.

2. Preparation methods

The preparation methods for bismuth titanate primarily include chemical solution deposition,[16,38] sol–gel method,[39–41] hydrothermal/solvothermal method,[42–44] self-assembly,[45] electrospinning,[46,47] calcination,[48] co-precipitation method,[49,50] molten salt method,[51,52] and solid-phase reaction method,[53] among others. Additionally, there are specialized or modified synthesis methods, such as the reverse micelle-templating method,[9] polymer precursor (Pechini) method,[54] aerosol-assisted self-assembly,[45] high-temperature quenching method,[18] *etc.* Several commonly used synthesis methods are highlighted below.

2.1 Chemical solution deposition

Chemical solvent techniques provide excellent separation and extraction efficiency and selectivity, but with drawbacks such as environmental toxicity, high energy consumption, and operational complexity. Yao *et al.*[16] used the chemical solution method to prepare $Bi_2Ti_2O_7$ nanoparticles which exhibited an excellent performance towards the degradation of methyl orange. Despite the gradual replacement of the chemical solution method by other synthesis methods in recent years, Qian *et al.*[55] capitalized on its advantages to successfully synthesize a novel $Bi_2Ti_2O_7$/$Bi_4Ti_3O_{12}$ heterostructure. The material exhibited a much smaller size than that prepared by solid-state reaction (*ca.* 500 nm) and excellent visible light absorption for the degradation of tetracycline hydrochloride.

2.2 Solvent gel method

The sol–gel method, as demonstrated by Dislich *et al.* in 1971,[56] enables molecular-level homogeneity and low-temperature synthesis of complex composites but suffers from prolonged aging and challenges in size control. Su *et al.*[23] dissolved bismuth nitrate, titanium tetrabutylate, and ammonia in glacial acetic acid, adjusted the pH, and dried it to obtain a transparent gel, which was then calcined to produce $Bi_2Ti_2O_7$ powders. To control the materials morphology, Zhou *et al.*[6] dissolved bismuth nitrate pentahydrate and isopropoxy titanium in an ice-acetic acid solution, and added 2-methoxyethanol to adjust the viscosity and surface tension of the prepared transparent sol. A porous anodic aluminium oxide template was soaked in the solution for 5 min, then heated and annealed by calcination before being dissolved in a NaOH solution for 24 h to separate the $Bi_2Ti_2O_7$ nanotubes, which exhibited a photocatalytic performance superior to that of the bulk counterpart prepared without a template towards the degradation of methyl orange, with an apparent reaction rate constant of *ca.* 6.88×10^{-3} and 3.62×10^{-3} min^{-1}, respectively. In another study, Chen *et al.*[57] employed the sol–gel hydrothermal technique to prepare single-crystal $Bi_4Ti_3O_{12}$ nanoplates with exposed {001} facets. This process was simple, template-free, surfactant-free, and energy-efficient.

2.3 Coprecipitation method

Coprecipitation method is a simple process that can refine and uniformly mix the raw materials to prepare samples of a low particle size. Li *et al.*[26] prepared $Bi_2Ti_2O_7$ particles of about 1–4 μm in diameter *via* the coprecipitation method using bismuth nitrate and tetra-*n*-butyl titanate as raw materials and acetic acid as the solvent. The particles possessed a high specific surface area and an enhanced degradation performance toward rhodamine B (RhB). Benčina *et al.*[22] successfully synthesized 90 nm $Bi_2Ti_2O_7$ nanocrystals by increasing the drying temperature and extending the duration of high-temperature annealing.

The coprecipitation method has also been used in combination with other synthesis techniques. Li *et al.*[19] used a two-step precipitation-infiltration method to synthesize an iodine-sensitized $Bi_4Ti_3O_{12}/TiO_2$ photocatalyst. The synthesis process consisted of two major steps. The first step involved the synthesis of a $Bi_4Ti_3O_{12}/TiO_2$ heterostructure using bismuth nitrate and titanium dioxide as raw materials *via* the precipitation method; and the second step involved infiltrating the $Bi_4Ti_3O_{12}/TiO_2$ heterostructure with an HI ethanol solution to prepare an iodine-sensitized $Bi_4Ti_3O_{12}/TiO_2$ catalyst. In a more recent study, Zhang *et al.*[15] first prepared perovskite $Bi_2Ti_2O_7$

through a conventional coprecipitation method and then synthesized defect-containing $Bi_2Ti_2O_7/TiO_2$ composites through *in situ* topological chemical etching. The process entailed the following steps. $Bi_2Ti_2O_7$ was placed on a ceramic wafer and calcined in a tube furnace under an atmosphere of argon and hydrogen. The obtained samples were then dispersed into nitric acid under stirring, centrifuged, rinsed with deionized water, and dried to obtain the $Bi_2Ti_2O_7/TiO_2$ photocatalyst, where $Bi_2Ti_2O_7$ was loaded onto defective TiO_2. This inhibited the reverse reaction during the photocatalytic conversion of CO_2 to CH_4, thereby improving the activity and selectivity of the catalyst.

Coprecipitation is a well-studied, relatively mature preparation method. However, issues remain, such as the potential for excessively high local concentrations upon the addition of the precipitating agents, which may lead to agglomeration and/or insufficient uniformity in the composition.

2.4 Electrospinning

Electrospinning is a versatile and cost-effective nanofiber fabrication technique that utilizes a high-voltage electric field to produce submicron-to-nanoscale continuous fibers (Fig. 2), offering advantages of simplicity, scalability, and precise control of fiber morphology.[58,59] In the preparation of bismuth titanate catalysts, electrospinning is typically combined with calcination. For instance, Hou *et al.*[60] fabricated porous $Bi_4Ti_3O_{12}$ nanofibers *via* electrospinning of a polyvinylpyrrolidone (PVP)-containing precursor solution, and demonstrated that calcination temperature critically determined the fiber morphology and the eventual RhB degradation performance.

Despite clear advantages as compared to other methods for nanofiber preparation, challenges remain with electrospinning in reducing the average fiber diameter to below 20 nm and in preparing nanofibers with porous or hollow structures to enhance the fiber surface area. Further study is desired.

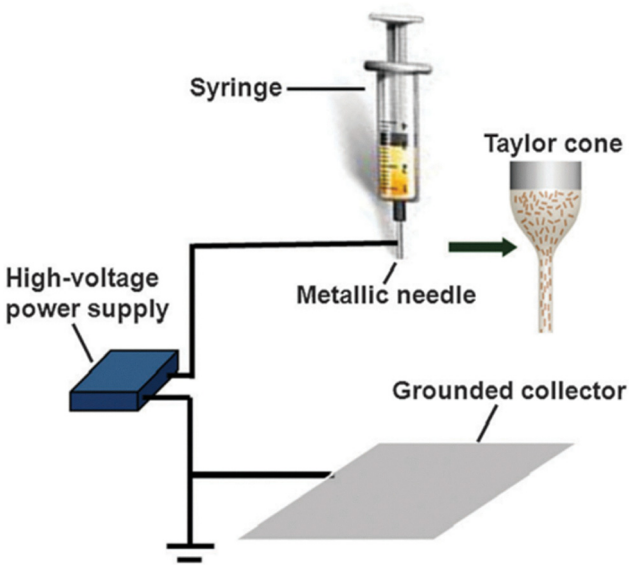

Fig. 2 Schematic diagram of electrospinning. Reproduced or adapted with permission from ref. 58. Copyright 1972 Royal Society of Chemistry.

2.5 Hydrothermal/solvothermal method

Hydrothermal/solvothermal synthesis produces well-crystallized, phase-pure nanomaterials with controlled morphology and enhanced sintering activity by employing solvent-mediated crystallization in closed systems at elevated temperatures/pressures while eliminating the need for post-synthesis calcination.[61] For instance, Niu *et al.*[62] synthesized BiOCl/$Bi_2Ti_2O_7$ heterostructures by hydrothermally processing a mixture of ultrasonically dispersed BiOCl nanosheets with other raw materials. Shi *et al.*[13] successfully fabricated $Bi_2Ti_2O_7$/$CaTiO_3$ heterostructures *via* a one-pot hydrothermal route under alkaline conditions, achieving effective deposition of $Bi_2Ti_2O_7$ nanoparticle on $CaTiO_3$ substrates. Due to the physicochemical properties of solvents like water and ethanol, hydrothermal/solvothermal synthesis is not suitable for high-temperature applications. Thus, it is sometimes necessary to combine it with other processes, such as calcination. Li *et al.*[63] added $Bi(NO_3)_3{\cdot}5H_2O$ and $Ti(C_4H_9O)_4$ to a glycerol/ethanol mixture at room temperature, stirred and sonicated appropriately, and then heated the mixture at 120 °C for 24 h. The dried samples were finally calcined at 600 °C for 3 h, successfully synthesizing a $Bi_2Ti_2O_7/TiO_2$/RGO composite material.

Overall, hydrothermal/solvothermal synthesis is a well-studied preparation method. Yet issues remain concerning precise control over the size, shape, and crystallinity of the nanomaterials, as well as challenges of large-scale production.

2.6 Other methods

The molten salt method enables morphology-controlled synthesis of bismuth titanates, as demonstrated by Ren *et al.*[64] who fabricated $Bi_4Ti_3O_{12}$ nanosheets from Bi_2O_3/TiO_2 precursors in KCl/NaCl molten salts (750 °C, 2 h) for the preparation of $ZnSnO_3/Bi_4Ti_3O_{12}$ composites. Wang *et al.*[52] further showed temperature-dependent facet control (800–900 °C) of $Bi_4Ti_3O_{12}$ nanosheets, which directly influenced the photocatalytic activity. Alternatively, Li *et al.*[48] prepared oxygen-deficient $Bi_2Ti_2O_7$/$CaTiO_3$ heterojunctions through a solvothermal–calcination dual process and observed an enhanced performance towards NO photodegradation. These methods collectively provide versatile pathways for tailoring the bismuth titanate nanostructures.

3. Morphology and structure

3.1 0D bismuth titanate

Common forms of 0D nanomaterials include nanoparticles, nanospheres, and quantum dots. The quantum confinement effect and high surface area-to-volume ratio endow 0D nanomaterials with excellent light absorption and high accessibility of reactive sites, leading to high photocatalytic activity. Hydrothermal,[13,62,65] precipitation,[15,22,66] solvothermal,[48,63,67,68] sol–gel,[69] molten salt,[70] templating,[71] and wet chemical methods[72,73] are common approaches to the synthesis of 0D $Bi_2Ti_2O_7$. For instance, Zhang *et al.*[15] constructed Type-II heterojunctions consisting of $Bi_2Ti_2O_7$ nanoparticles and defective TiO_2, which achieved 93.5% CH_4 selectivity in CO_2 reduction

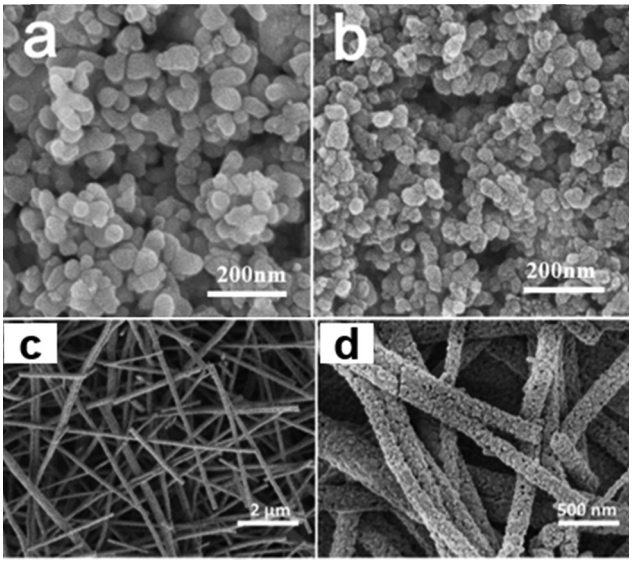

Fig. 3 SEM images of (a) BTO and (b) BTO/TiO_2-500. Reproduced or adapted with permission from ref. 34. Copyright 2022 Elsevier. (c) and (d) SEM patterns of N-Fe-BTO 0.5% samples. Reproduced or adapted with permission from ref. 27. Copyright (CC-BY 4.0) 2016 Springer Link.

due to enhanced charge separation efficiency (Fig. 3a and b). Furthermore, many studies have employed a one-pot hydrothermal method by directly adding bismuth and titanium sources to the precursor solutions of other materials, resulting in 0D $Bi_2Ti_2O_7$ adhering to the surfaces of other materials to produce $Bi_2Ti_2O_7$ composite photocatalysts with an enhanced performance.[13,62,74]

3.2 1D bismuth titanate

1D $Bi_2Ti_2O_7$ has been commonly produced by techniques such as solvothermal[75] and sol–gel methods.[6] Electrospinning[2,27,76,77] is also considered as a simpler and more efficient synthetic technique as compared to the preparation of the 0D counterparts. Zhou *et al.*[6] synthesized $Bi_2Ti_2O_7$ nanotubes (180–330 nm diameter, 6 nm wall thickness) *via* a templated sol–gel method, while Liu *et al.*[27] developed Fe/N-co-doped nanofibers (100–150 nm diameter, Fig. 3c and d) through electrospinning and nitridation, which possessed a high surface area and abundant catalytic active sites for enhanced photocatalysis. The 1D $Bi_2Ti_2O_7$ nanomaterials can offer efficient charge separation and rapid transport in photocatalysis, significantly enhancing the photocatalytic activity.

3.3 2D bismuth titanate

Nanosheets are a common type of 2D nanomaterial, characterized by large planar dimensions, small thickness, large specific surface area, and short carrier migration distances, making them ideal candidates for efficient photocatalytic systems. For instance, Liu *et al.*[78] prepared $Bi_2Ti_2O_7/\gamma$-Bi_2O_3 composites (Fig. 4a–g) *via in situ* hydrothermal growth that consisted of $Bi_2Ti_2O_7$ nanosheets (10 nm thick, Fig. 4b–d) vertically aligned on γ-Bi_2O_3 substrates. Du *et al.*[79] demonstrated that the $Bi_2Ti_2O_7/Bi_4Ti_3O_{12}$ morphology and hence photocatalytic performance could be manipulated by calcination temperature

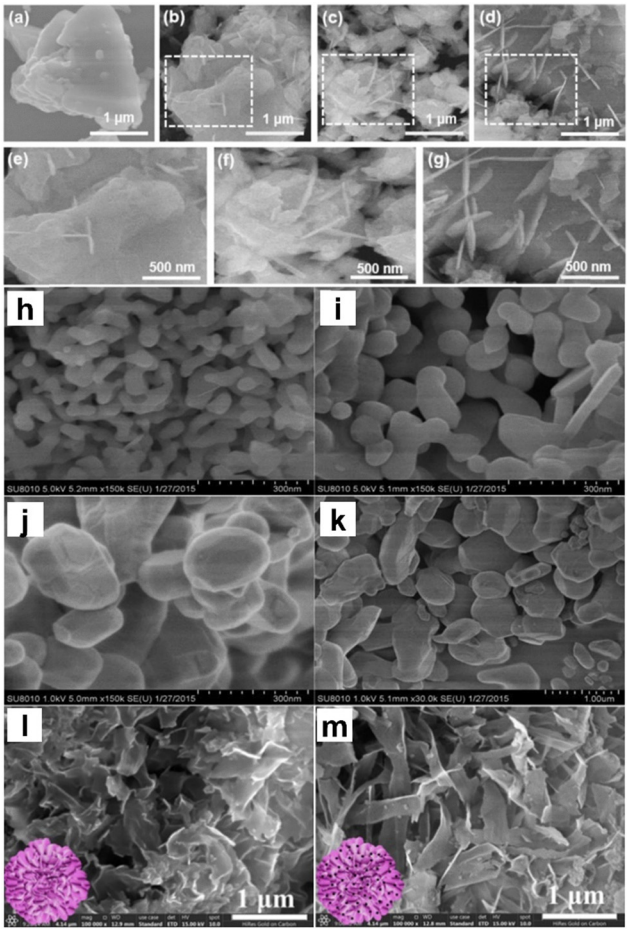

Fig. 4 SEM images of (a) γ-Bi_2O_3, (b, e) 0.5% BT/γ-Bi_2O_3, (c, f) 3% BT/γ-Bi_2O_3, and (d, g) 7% BT/γ-Bi_2O_3. Reproduced or adapted with permission from ref. 78. Copyright 2019 Elsevier. (h) SEM images of $Bi_2Ti_2O_7/Bi_4Ti_3O_{12}$ nanocomposites prepared at (a) 500, (i) 600, (j) 700 and (k) 800 °C. Reproduced or adapted with permission from ref. 79. Copyright 2017 Elsevier. SEM images of (l) $Bi_2Ti_2O_7$ and (m) Bi@$Bi_2Ti_2O_7$-OV-4 (with the addition of 0.4 g glucose). The inserts in (l) and (m) are their structure cartoons. Reproduced or adapted with permission from ref. 14. Copyright 2022 Elsevier.

(Fig. 4h–k). Specifically, worm-like nanosheets (100–200 nm length, 20 nm thick, Fig. 4i) were produced at 600 °C, achieved an RhB degradation rate 2× higher than that of pure $Bi_2Ti_2O_7$; yet at higher calcination temperatures, the band gap became enlarged to 2.92 eV at 700 °C and 3.04 eV at 800 °C, which greatly limited the visible light absorption and photocatalytic activity.

Despite substantial research progress, there remains a long way to go before 2D $Bi_2Ti_2O_7$ can be applied industrially on a large scale. Currently, studies of photocatalysis of 2D $Bi_2Ti_2O_7$ are primarily focused on improving the photocatalytic performance while ensuring material stability.

3.4 3D bismuth titanate

3D $Bi_2Ti_2O_7$ nanostructures typically exhibit a high specific surface area, high porosity, high permeability, and excellent anti-agglomeration capability. Furthermore, layered structures

can increase the number of light propagation paths and facilitate charge carrier transport, thereby promoting photo absorption and enhancing charge separation efficiency. Zhu *et al.*[14] synthesized oxygen-deficient $Bi_2Ti_2O_7$ nanothin films using a one-pot hydrothermal method with glucose as the reducing agent. The addition of glucose resulted in the reduction of some Bi^{3+} to metallic Bi, which was then loaded onto the nanothin films. As shown in Fig. 4l and m, both $Bi_2Ti_2O_7$ and Bi-$Bi_2Ti_2O_7$ self-assembled into 3D porous nanosheets. Adjusting the amount of glucose added could control the loading of bismuth on the surface of $Bi_2Ti_2O_7$. With an increasing amount of glucose added, the specific surface area and pore volume of the photocatalysts gradually increased, providing more active sites and enhancing the light absorption capability of the photocatalysts. Zhong *et al.*[37] successfully prepared an efficient visible light-driven spherical photocatalyst Ag@AgCl/$Bi_2Ti_2O_7$ using solvothermal and subsequent deposition–precipitation/co-sintering processes. The 3D nanostructure of $Bi_2Ti_2O_7$ facilitated the deposition of AgCl particles, and the synergistic effect of surface plasmon resonance (SPR) of Ag^0 generated from photoreduction of AgCl impeded the recombination of photoinduced charge carriers by transferring electrons from Ag^0 to $Bi_2Ti_2O_7$, thereby enhancing the visible-light photocatalytic activity of Ag@AgCl/$Bi_2Ti_2O_7$. Liu *et al.*[24] successfully synthesized $Bi_2Ti_2O_7$ materials with a nano-microsphere structure of *ca.* 2–5 mm in diameter by calcination at 600 °C. After modification with nitrogen-doped graphene quantum dots (N-GQD), the N-GQD/$Bi_2Ti_2O_7$ microspheres exhibited multi-level effects and activation zones, which led to enhanced photocatalytic performance. The modification with N-GQD also enhanced the separation efficiency of the electron–hole pairs.

Overall, calcination, hydrothermal, and solvothermal methods are the most commonly used techniques to synthesize $Bi_2Ti_2O_7$ of varied morphologies. By altering the feed ratios of the bismuth and titanium sources, reaction time and temperature, and the addition of additives, the size and morphology of the obtained bismuth titanate can be readily controlled. In calcination, the reaction temperature can significantly affect the size and dispersion of bismuth titanate. In hydrothermal and solvothermal methods, the acidity or alkalinity also plays a key role in influencing the size and morphology of the products.[80]

4. Modification strategies

Despite significant advantages of $Bi_2Ti_2O_7$-based photocatalysts, pure-phase $Bi_2Ti_2O_7$ suffers from a limited range of light absorption, high rate of carrier recombination, and poor stability. These issues can be mitigated by a range of modification strategies, among which elemental doping, heterojunction engineering, and noble metal deposition are the most studied.

4.1 Elemental doping

Elemental doping plays a crucial role in enhancing and optimizing the photocatalytic performance of $Bi_2Ti_2O_7$. Doping can effectively adjust the electronic structure, surface properties, and bandgap energy of $Bi_2Ti_2O_7$, thereby improving its activity, stability, and light response range in photocatalytic reactions. For example, Jayaraman *et al.*[67] demonstrated that Cu/Fe co-doping reduced $Bi_2Ti_2O_7$ grain size from 68 to 45 nm and induced 3D nanostructure assembly, enhancing surface area and visible-light absorption *via* intermediate band formation (bandgap narrowing). Liu *et al.*[27] showed that Fe doping facilitated $Bi_4Ti_3O_{12}$ phase formation, creating Type-II heterojunctions for improved charge separation, while Krasnov *et al.*[81] and Mayfield *et al.*[82] showed that Cr/Mn/Fe doping introduced lattice distortions and oxygen vacancies, further optimizing the photocatalytic activity.

Extensive research has also shown that doping of halogen elements can significantly enhance the photocatalytic performance of Bi-based materials.[83,84] Yet research on the impacts on bismuth titanate has remained scarce thus far. Further studies are desired.

4.2 Heterojunction engineering

To date, constructing appropriate heterojunctions between bismuth titanate and other semiconductor materials has been proven to be an effective strategy to enhance the photocatalytic performance.[85] The advantages of photocatalytic heterojunction structures are primarily manifested in the following aspects:

(1) Enhanced light absorption capability. Heterojunctions can absorb a broad spectrum of light, including visible and ultraviolet light. This allows for greater utilization of sunlight, increasing the opportunity to generate electron–hole pairs.

(2) Efficient carrier separation and migration. In heterojunctions, the difference in band structures between the two materials (such as band gaps and the relative positions of the conduction and valence bands) can facilitate effective separation of photogenerated electrons and holes. The CB of one material may serve as a dominant transmission channel for electrons, while the VB of another material provides a pathway for holes. This separation reduces the recombination rate of the electron–hole pairs, thereby increasing the number of effective reaction active sites.

(3) Enhanced surface reaction activity. Newly formed active sites at the heterojunction interface can serve as effective centers for catalytic reactions. For instance, during pollutant treatment, certain parts of the heterojunction may be more suitable for adsorbing specific reactants or intermediates and enhance the catalytic activity.

(4) Improved thermal and chemical stability. The formation of heterojunctions can enhance the material's thermal stability and corrosion resistance, which is crucial for maintaining the catalytic efficiency and lifespan under harsh conditions. Heterojunction photocatalysts, based on their band alignment, can primarily be classified into several types, such as Type-I/II, p–n, and Z-scheme, among others.[85]

The construction of heterojunctions has proven instrumental in addressing the inherent limitations of $Bi_2Ti_2O_7$ photocatalysts, particularly in enhancing charge separation and light

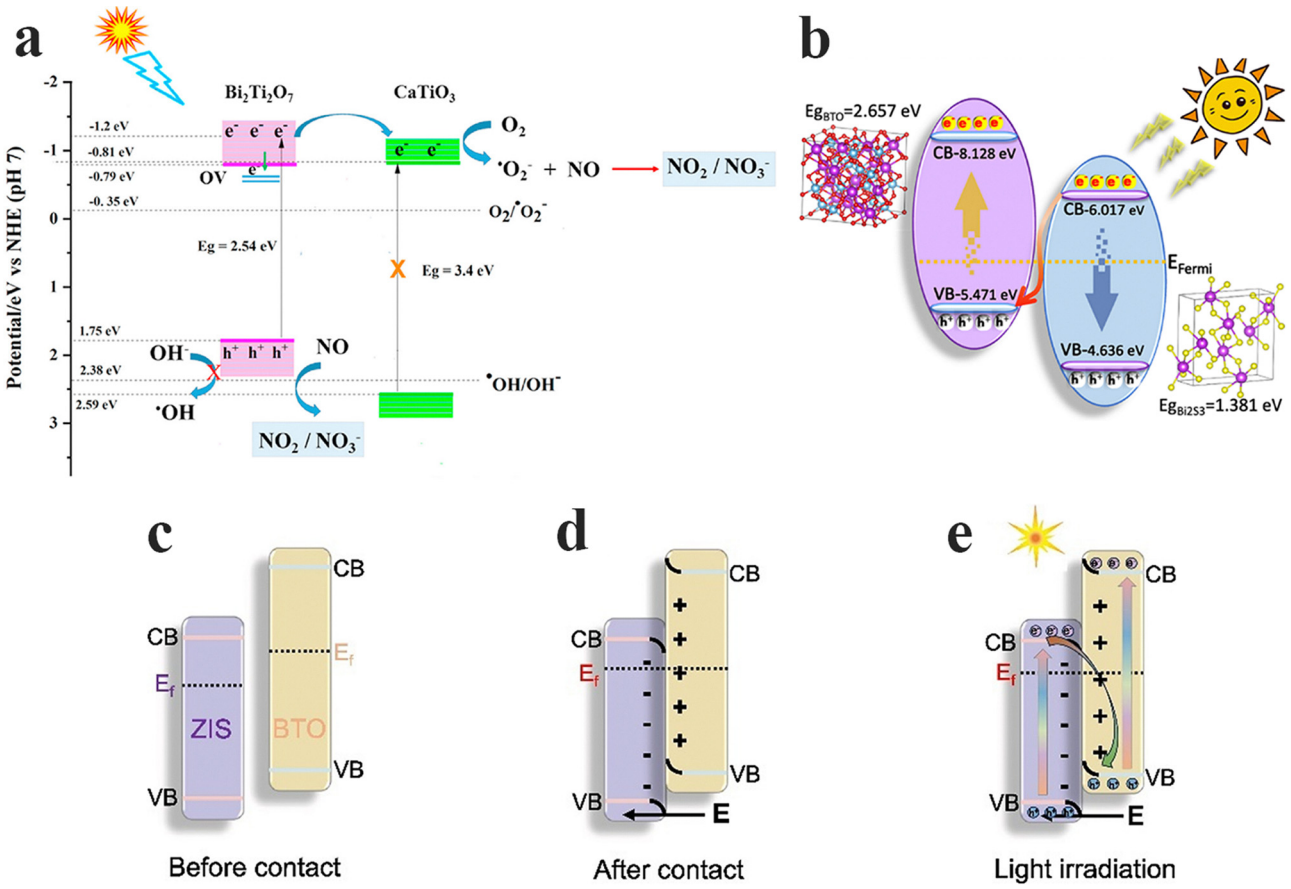

Fig. 5 (a) Schematic illustration of the proposed mechanism for photocatalytic removal of NO by BTO/CTO-2. Reproduced or adapted with permission from ref. 13. Copyright 2021 Elsevier. (b) Z-scheme diagram of a BTO@Bi_2S_3 photocatalyst. Reproduced or adapted with permission from ref. 36. Copyright 2023 Elsevier. Photocatalytic reaction mechanism of ZMB-20: (c) before contact, (d) after contact and (e) under light irradiation. Reproduced or adapted with permission from ref. 86. Copyright 2024 Elsevier.

absorption. Among the various heterojunction types, Type-II, Z-scheme, and S-scheme architectures have demonstrated remarkable promise.

Type-II heterojunctions, such as $Bi_2Ti_2O_7$/$CaTiO_3$, leverage staggered band alignment to spatially separate charge carriers. For instance, Shi *et al.*[13] synthesized $Bi_2Ti_2O_7$/$CaTiO_3$ composites *via* hydrothermal methods (Fig. 5a), where electrons migrated from the CB of $Bi_2Ti_2O_7$ that was slightly more negative than that of $CaTiO_3$ (−0.81 eV), while holes remained on the VB of $Bi_2Ti_2O_7$ (+1.75 eV). This configuration achieved 59% NO removal efficiency, doubling the performance of pure $Bi_2Ti_2O_7$, by minimizing carrier recombination. However, the redox potential is often compromised due to charge accumulation at lower-energy bands.

In contrast, Z-scheme heterojunctions retain strong redox capabilities through interfacial electric fields. Liu *et al.*[36] prepared $Bi_2Ti_2O_7$@Bi_2S_3 Z-scheme junctions (Fig. 5b), where DFT calculations confirmed charge density accumulation at the interface, driving the transfer of photogenerated electrons from the CB of Bi_2S_3 to the VB of $Bi_2Ti_2O_7$. The electrons in the CB of $Bi_2Ti_2O_7$ and holes in the VB of Bi_2S_3 enabled 82.08% oxytetracycline degradation within 150 min, outperforming Type-II systems by 2 times.

S-scheme heterojunctions further optimize charge dynamics *via* Fermi-level alignment. Ding *et al.*[86] developed $ZnIn_2S_4$/$Bi_4Ti_3O_{12}$ S-scheme composites (Fig. 5c–e), where electrons in the CB of $ZnIn_2S_4$ recombined with holes in the VB of $Bi_4Ti_3O_{12}$ under an internal electric field, leaving highly reductive electrons in the CB of $Bi_4Ti_3O_{12}$ (−0.6 eV). This design achieved a remarkable H_2 evolution rate of 27.5 mmol g^{-1} h^{-1} under visible light irradiation. In a recent study, Li *et al.*[87] demonstrated that the AgBr/$Bi_4Ti_3O_{12}$/$Bi_2Ti_2O_7$ ternary S-scheme heterojunction achieved a 13-fold increase of the RhB degradation rate and 81.04% Cr(VI) reduction efficiency through dual-channel charge transfer. A built-in electric field (IEF) selectively recombined low-energy carriers while preserving high-energy electrons for redox reactions, and $Bi_2Ti_2O_7$ extended visible-light absorption, addressing recombination and spectral limitations for scalable pollutant removal.

4.3 Noble metal deposition

In photocatalysis, the incorporation of noble metals into the catalysts has been demonstrated to confer several significant advantages. Firstly, the loading of noble metals can effectively enhance charge separation, thereby prolonging the lifetime of excited-state electrons and significantly reducing the probability

of recombination between photogenerated electrons and holes. This, in turn, provides a greater number of active charge carriers for photocatalytic reactions. Secondly, when noble metals come into contact with semiconductors, a Schottky barrier is formed, which can facilitate the formation of an efficient electron transfer channel, accelerate the rate of electron transfer and thus enhance the overall efficiency of photocatalytic reactions. Thirdly, noble metals can narrow the bandgap of semiconductors. This enables the materials to absorb light across a wider wavelength range, significantly improving the utilization efficiency of the photo energy. Fourthly, based on the SPR effect, noble metals can enhance light absorption, thereby effectively improving the light-harvesting capacity of the photocatalytic materials. Additionally, noble metals can also enhance the selectivity and activity of the catalytic reactions, precisely promoting the progress of target reactions and further optimizing the overall photocatalytic performance. For instance, Zhong *et al.*[37] successfully deposited AgCl particles on the surface of $Bi_2Ti_2O_7$ by combining a solvothermal method with a deposition–precipitation and co-sintering process. Under visible light irradiation, a portion of Ag^+ in AgCl was reduced to Ag^0, resulting in the formation of an Ag@AgCl/$Bi_2Ti_2O_7$ catalyst. The SPR effect of Ag^0 facilitated the transfer of electrons from the Ag^0 surface to $Bi_2Ti_2O_7$, thereby reducing the recombination rate of photogenerated carriers and enhancing the visible-light photocatalytic activity of AgCl/$Bi_2Ti_2O_7$. This was evidenced by the complete degradation of an RhB solution within 20 min's visible light photoirradiation. Li *et al.*[88] anchored Au nanorods on $Bi_4Ti_3O_{12}$, and leveraged SPR to broaden light absorption and transfer plasmon-induced hot electrons to the {001} facets of $Bi_4Ti_3O_{12}$, which synergistically enhanced the RhB degradation efficiency to almost 100% within 20 min.

5. Photocatalytic applications

Photocatalysis has become a widely applied key technology. In recent years, $Bi_2Ti_2O_7$ photocatalysts have been extensively used in areas such as removal of water pollutants, hydrogen production, and CO_2 reduction (Table 1). Among these, the most frequent applications are photocatalytic removal of water pollutants, nitric oxide removal, and hydrogen generation. This section will summarize their advanced applications in these areas.

5.1 Photocatalytic removal of pollutants in water

Photocatalytic degradation of pollutants in water is essentially an application of advanced oxidation technology. By simulating sunlight or daylight, various radicals are generated to transform large, non-degradable organic molecules in water into smaller molecules, ultimately achieving complete mineralization and thereby purification of water.[89] In bismuth titanate photocatalysts the interactions between the Bi 6s and O 2p orbitals enhance the migration of photogenerated holes and result in effective photocatalytic activation.[73] It has been found that h^+ and $O_2^{\bullet-}$ radicals play a primary role in the degradation of organic dyes and antibiotics,[24,36,65] with synergistic contributions from $^\bullet OH$ radicals.[63,90] In fact, the addition of persul-

Table 1 Summary of photocatalytic performance of bismuth titanate

Application	Catalyst system	Performance	Key mechanism	Ref.
Pollutant degradation	$Bi_2Ti_2O_7$/persulfate	88.2% tetracycline degradation (150 min, visible light)	Persulfate activates $^\bullet OH$/$^\bullet O_2^-$ radicals; synergistic charge separation	Liu *et al.*[65]
	$Bi_2Ti_2O_7$@Bi_2S_3/PU sponge	82.08% oxytetracycline removal (180 min)	Z-scheme heterojunction optimizes band structure; Bi^{3+}/Bi^{5+} and Ti^{4+}/Ti^{3+} redox cycles enhance charge transfer	Liu *et al.*[36]
	Cu,Fe-$Bi_2Ti_2O_7$/EG-g-C_3N_4	69.5% ciprofloxacin and 83.69% rhodamine B degradation	Co-doping introduces mid-gap states; EG-g-C_3N_4 porous structure improves adsorption/light absorption	Venkatesan *et al.*[92]
	$Bi_2Ti_2O_7$/TiO_2/RGO	95% ciprofloxacin degradation (180 min, simulated sunlight)	RGO prevents agglomeration; ternary heterojunction enhances charge separation	Li *et al.*[63]
	BiOCl/$Bi_2Ti_2O_7$ nanorods	Efficient tetracycline hydrochloride degradation	Electrospinning-built heterojunction; narrow bandgap $Bi_2Ti_2O_7$ boosts solar utilization	Xu *et al.*[76]
NO removal	$Bi_2Ti_2O_7$/$CaTiO_3$ heterojunction	59% NO removal (600 ppb, visible light)	Oxygen vacancies enhance visible-light absorption; heterojunction improves charge separation	Shi *et al.*[13]
	Oxygen vacancy/Bi SPR-$Bi_2Ti_2O_7$	79% NO removal (full-spectrum), 2.5× higher than pristine $Bi_2Ti_2O_7$ (31.79%)	Oxygen vacancies tune bandgap; Bi SPR extends NIR response and inhibits toxic intermediates	Zhu *et al.*[14]
H_2 production	Fe-doped $Bi_2Ti_2O_7$	75% higher H_2 evolution rate (visible light, methanol sacrificial agent)	Fe doping creates mid-gap states to optimize electron migration paths	Allured *et al.*[73]
	g-C_3N_4/$Bi_4Ti_3O_{12}$/$Bi_2Ti_2O_7$	638 μmol g^{-1} H_2 (760% higher than binary composite)	Ternary heterojunction suppresses recombination; g-C_3N_4 extends light absorption	Zhao *et al.*[77]
CO_2 reduction	Defective $Bi_2Ti_2O_7$/TiO_2	6.8 μmol g^{-1} h^{-1} CH_4 (93.5% selectivity; 7.9 × higher than P25 TiO_2)	Oxygen vacancies adsorb CO_2; Type-II heterojunction suppresses reverse reactions	Zhang *et al.*[34]
	$Bi_2Ti_2O_7$ (O 2p–Bi 6s hybridized)	High CH_4 selectivity	Hybridized VBM facilitates electron donation to CO_2, forming stable carbonate intermediates	Walker *et al.*[93]
Other applications	$Bi_2Ti_2O_7$ quantum dots (vacancies)	77 × higher NH_3 yield *vs.* bulk	Quantum confinement + oxygen vacancies enhance N_2 adsorption/activation	Li *et al.*[94]
	$Bi_2Ti_2O_7$/γ-Bi_2O_3 hierarchical	Efficient phenol and dye degradation	Shared Bi–O tetrahedral units enable atomic-level charge transfer pathways	Liu *et al.*[78]

fates (such as potassium persulfate and ammonium persulfate) can enhance the degradation efficiency of antibiotics in photocatalytic processes by the generation of strongly oxidizing $^{\bullet}OH$. Liu *et al.*[65] observed 88.2% removal of tetracycline within 150 min under visible light using a $Bi_2Ti_2O_7$/persulfate system. The persulfate synergistically enhanced charge separation and activated radicals (*e.g.*, $^{\bullet}OH$, $O_2^{\bullet-}$), significantly boosting the oxidative capacity. This strategy provided a novel approach for industrial wastewater treatment, though the long-term stability of the catalytic system requires further optimization. Furthermore, the photo-Fenton reaction, due to its high efficiency and solar energy utilization rate that leads to a reduced operational cost, has been recognized as a sustainable water treatment technology, where $Bi_2Ti_2O_7$ has emerged as a viable photocatalyst.[1]

5.2 Photocatalytic removal of nitric oxide

$Bi_2Ti_2O_7$ can generate electron–hole pairs under ultraviolet or visible light irradiation, producing strong oxidants such as hydroxyl radicals ($^{\bullet}OH$), which effectively oxidize NO (a major air pollutant from vehicle exhaust and industrial emissions) into harmless substances. For instance, Shi *et al.*[13] synthesized a visible light-driven $Bi_2Ti_2O_7/CaTiO_3$ heterojunction *via* an *in situ* hydrothermal method, achieving a 59% NO removal efficiency at 20 wt% $Bi_2Ti_2O_7$ under visible light irradiation of 600 ppb NO, outperforming pure $CaTiO_3$ and $Bi_2Ti_2O_7$. Zhu *et al.*[14] developed full-spectrum $Bi_2Ti_2O_7$ with oxygen vacancies using a one-pot hydrothermal method. The introduction of SPR metals and oxygen vacancies enhanced visible-near-infrared light photocatalytic activity, achieving a 79% NO removal efficiency that was more than double that of pristine $Bi_2Ti_2O_7$ (31.79%). Both studies demonstrated advancements in air purification, although scalability and stability under real-world conditions require further validation.

5.3 Photocatalytic hydrogen production

In photocatalytic hydrogen production, semiconductor materials absorb solar energy to generate electron–hole pairs, which possess strong redox capabilities towards the splitting of water molecules to hydrogen and oxygen.[91] Key processes in photocatalytic hydrogen production include semiconductor excitation by sunlight to create electron–hole pairs, followed by partial recombination of these pairs, with separated electrons and holes migrating to the surface of the semiconductor material. On the material surface, the photoinduced holes oxidize water molecules to produce oxygen, while photoinduced electrons reduce water molecules to generate hydrogen. For instance, Allured *et al.*[73] incorporated Fe into $Bi_2Ti_2O_7$ *via* a wet chemical method, where Fe substitution at the Bi/Ti sites led to the formation of intermediate energy bands between the VB and CB. This modification increased the hydrogen evolution rate by 75% as compared to that by undoped $Bi_2Ti_2O_7$ under visible light irradiation with methanol as a sacrificial agent. Zhao *et al.*[77] developed a g-$C_3N_4/Bi_4Ti_3O_{12}/Bi_2Ti_2O_7$ ternary heterojunction *via* electrospinning and calcination, achieving a hydrogen production rate of 638 mmol g^{-1} under visible light, which was 760% higher than $Bi_4Ti_3O_{12}/Bi_2Ti_2O_7$ nanofibers and 55% higher than pristine g-C_3N_4. The enhanced performance was attributed to improved charge separation and extended light absorption.

5.4 Photocatalytic reduction of carbon dioxide

Photocatalytic CO_2 reduction represents a promising strategy for converting greenhouse gases into value-added fuels, such as methane (CH_4) and carbon monoxide (CO) by utilizing solar energy. Bismuth titanate-based materials, particularly $Bi_2Ti_2O_7$, have garnered significant attention due to their unique surface chemistry and tunable electronic structure, which enhance CO_2 adsorption and activation. Zhang *et al.*[34] developed a defective $Bi_2Ti_2O_7/TiO_2$ heterostructure *via* an *in situ* topochemical reaction etching route. The composite exhibited a CH_4 production rate of 6.8 μmol g^{-1} h^{-1} under visible light irradiation, 7.9 times higher than that of commercial P25 TiO_2, with 93.5% selectivity toward CH_4. The enhanced performance was attributed to oxygen vacancies in TiO_2, which provided abundant active sites for CO_2 adsorption, and the formation of a Type-II heterojunction between $Bi_2Ti_2O_7$ and TiO_2, which promoted charge separation and suppressed hydroxyl radical-induced reverse reactions. Furthermore, Walker *et al.*[93] demonstrated that the O 2p–Bi 6s/6p hybridized states at the valence band maximum (VBM) enhance electron donation to adsorbed CO_2, favoring the formation of stable carbonate intermediates. *In situ* diffuse reflectance IR spectroscopy (DRIFTS) measurements revealed that $Bi_2Ti_2O_7$ surfaces predominantly host monodentate and bidentate carbonate species, which are critical precursors for CH_4 generation.

5.5 Other applications

Beyond the above-mentioned applications, bismuth titanate has also shown promise in photocatalytic nitrogen fixation and H_2O_2 production.[95] Li *et al.*[94] synthesized $Bi_2Ti_2O_7$ quantum dots *via* mannitol-assisted size confinement, where oxygen vacancies generated shallow energy levels. The synergy with the quantum confinement effects enhanced charge carrier mobility and separation, enabling efficient nitrogen molecule adsorption/activation. The optimized quantum dots achieved a 77-fold increase of the nitrogen fixation efficiency as compared to bulk $Bi_2Ti_2O_7$. Future efforts should focus on engineering oxygen vacancies with controlled energy levels (shallow over deep) to maximize the catalytic activity, which may be a strategic direction for advancing $Bi_2Ti_2O_7$-based photocatalysts.

6. Conclusions and perspectives

In summary, bismuth titanate has emerged as an attractive photocatalyst due to unique crystal and electronic band structures and demonstrated significant and broad applications in diverse areas of interest. Thus far, a wide range of effective methods have been successfully developed for the preparation of bismuth titanate of controlled morphologies. In addition, various strategies have been reported for the deliberate

engineering of the material structures, a critical step towards the optimization of the photocatalytic performance.

Despite significant progress, several challenges remain in $Bi_2Ti_2O_7$-based photocatalysis. Firstly, while $Bi_2Ti_2O_7$ demonstrates a remarkable photocatalytic performance, the light absorption range remains largely confined to the ultraviolet region, which limits the photocatalytic efficiency. Therefore, expanding the photo absorption of $Bi_2Ti_2O_7$ to the visible range remains a key focus in continuing research. Additionally, the photocatalytic performance of $Bi_2Ti_2O_7$ is significantly impacted by the relatively high rate of carrier recombination. Thus, effective strategies to impede carrier recombination are critically needed, among which defect engineering represents a viable tool.

In addition, integrating machine learning (ML)-enabled spectroscopic analysis into $Bi_2Ti_2O_7$ photocatalysis research offers a transformative approach to accelerating the screening of bismuth titanate-based composites (*e.g.*, heterojunctions, defect-engineered materials) and inversely design catalysts with tailored adsorption/activation capabilities. This may advance the understanding of the microscopic mechanisms of charge transfer and intermediate evolution in $Bi_2Ti_2O_7$ photocatalysis, key limitations in conventional experimental characterization. Such integration holds promise for establishing a closed-loop optimization framework by connecting material synthesis and structural features with catalytic performance, thereby advancing the rational design and performance optimization of the photocatalysts.

Author contributions

Xiang Sui, Runjie Wu, Mingming Sun, Ming Guo, Zeping Qin, Pengkun Li, Xingrui Liu, and Davida Briana DuBois: investigation, writing – original draft; Shaowei Chen and Qiang Wang: conceptualization, writing – review & editing.

Conflicts of interest

There are no conflicts to declare.

Data availability

No new data were generated as part of this review.

Acknowledgements

This work was supported by the Natural Science Foundation of China (NSFC, 52372212). S. W. C. thanks the National Science Foundation for partial support of the work (CHE-2003685).

References

1 C. Du, Y. Zhang, Z. Zhang, L. Zhou, G. Yu, X. Wen, T. Chi, G. Wang, Y. Su, F. Deng, Y. Lv and H. Zhu, *Chem. Eng. J.*, 2022, **431**, 133932.
2 H. Shi, H. Tan, W.-B. Zhu, Z. Sun, Y. Ma and E. Wang, *J. Mater. Chem. A*, 2015, **3**, 6586–6591.
3 M. Rostami, A. Badiei, M. R. Ganjali, M. Rahimi-Nasrabadi, M. Naddafi and H. Karimi-Maleh, *Environ. Res.*, 2022, **212**, 113347.
4 I. Nabi, A.-U.-R. Bacha, F. Ahmad and L. Zhang, *J. Environ. Chem. Eng.*, 2021, **9**, 105964.
5 P. Hao, Z. H. Zhao, J. Tian, Y. H. Sang, G. W. Yu, H. Liu, S. W. Chen and W. J. Zhou, *Acta Mater.*, 2014, **62**, 258–266.
6 H. Zhou, T.-J. Park and S. S. Wong, *J. Mater. Res.*, 2011, **21**, 2941–2947.
7 A. G. Krasnov, M. S. Napalkov, M. I. Vlasov, M. S. Koroleva, I. R. Shein and I. V. Piir, *Inorg. Chem.*, 2020, **59**, 12385–12396.
8 V. Kumar, R. Sharma, S. Kumar, M. Kaur and J. D. Sharma, *Ceram. Int.*, 2019, **45**, 20386–20395.
9 S. Murugesan and V. R. Subramanian, *Chem. Commun.*, 2009, 5109–5111.
10 S. Gupta and V. R. Subramanian, *ACS Appl. Mater. Interfaces*, 2014, **6**, 18597–18608.
11 O. Merka, D. W. Bahnemann and M. Wark, *Catal. Today*, 2014, **225**, 102–110.
12 D. Du, M. Shi, Q. Guo, Y. Zhang, A. A. Allam, A. Rady and C. Wang, *Catalysts*, 2023, **13**, 1169.
13 M. Shi, B. Rhimi, K. Zhang, J. Xu, D. W. Bahnemann and C. Wang, *Chemosphere*, 2021, **275**, 130083.
14 Q. Zhu, R. Hailili, Y. Xin, Y. Zhou, Y. Huang, X. Pang, K. Zhang, P. K. J. Robertson, D. W. Bahnemann and C. Wang, *Appl. Catal., B*, 2022, **319**, 121888.
15 D. Zhang, Y. J. Sun, X. Tian, X. T. Liu, X. J. Wang, J. Zhao, Y. P. Li and F. T. Li, *J. Colloid Interface Sci.*, 2022, **606**, 1477–1487.
16 W. Yao, *Appl. Catal., A*, 2004, **259**, 29–33.
17 H. Zhang, M. Lü, S. Liu, Z. Xiu, G. Zhou, Y. Zhou, Z. Qiu, A. Zhang and Q. Ma, *Surf. Coat. Technol.*, 2008, **202**, 4930–4934.
18 H. Cheng, B. Huang, Y. Dai, X. Qin, X. Zhang, Z. Wang and M. Jiang, *J. Solid State Chem.*, 2009, **182**, 2274–2278.
19 Y. Li, L. Dang, L. Han, P. Li, J. Wang and Z. Li, *J. Mol. Catal. A: Chem.*, 2013, **379**, 146–151.
20 W. W. Zhao, C. Y. Zhang, Y. W. Liu, X. P. Huang and F. Mao, *Adv. Mater.*, 2011, **306**, 1416–1419.
21 X. Feng, J. Xu, X. Xu, S. Zhang, J. Ma, X. Fang and X. Wang, *ACS Catal.*, 2021, **11**, 12112–12122.
22 M. Benčina and M. Valant, *J. Am. Ceram. Soc.*, 2017, **101**, 82–90.
23 X. L. Su and Y. C. Zhang, *Adv. Mater. Res.*, 2012, **412**, 103–106.
24 X. Liu, Z. Zhou, T. Wang, C. Ma and Y. Yan, *J. Dispersion Sci. Technol.*, 2020, **43**, 639–648.
25 T. Wang, X. Liu, Q. Men, W. Ma, Z. Liu, Y. Liu, C. Ma, P. Huo and Y. Yan, *Spectrochim. Acta, Part A*, 2019, **213**, 19–27.
26 Y.-F. Li, Y. Zhong, J.-Q. Chang and C.-H. Hu, *IOP Conf. Ser.: Mater. Sci. Eng.*, 2018, **307**, 012041.
27 B. Liu, Q. Mo, J. Zhu, Z. Hou, L. Peng, Y. Tu and Q. Wang, *Nanoscale Res. Lett.*, 2016, **11**, 391.
28 H. Zhang, M. Lü, S. liu, X. Song, Y. Zhou, Z. Xiu, Z. Qiu, A. Zhang and Q. Ma, *Thin Solid Films*, 2008, **517**, 764–768.
29 D. Li, H. Song, X. Meng, T. Shen, J. Sun, W. Han and X. Wang, *Nanomaterials*, 2020, **10**, 546.
30 X. Yang, H. Tao, W. R. Leow, J. Li, Y. Tan, Y. Zhang, T. Zhang, X. Chen, S. Gao and R. Cao, *J. Catal.*, 2019, **373**, 116–125.
31 P. Zhang, T. Wang, X. Chang and J. Gong, *Acc. Chem. Res.*, 2016, **49**, 911–921.
32 J. Yu and A. Kudo, *Adv. Funct. Mater.*, 2006, **16**, 2163–2169.
33 A. G. Krasnov, I. R. Shein, I. V. Piir and Y. I. Ryabkov, *Solid State Ionics*, 2018, **317**, 183–189.
34 D. Zhang, Y. J. Sun, X. Tian, X. T. Liu, X. J. Wang, J. Zhao, Y. P. Li and F. T. Li, *J. Colloid Interface Sci.*, 2022, **606**, 1477–1487.
35 G. A. Kallawar, D. P. Barai and B. A. Bhanvase, *J. Cleaner Prod.*, 2021, **318**, 128563.
36 Y. Liu, T. Hu, S. He, L. Feng, Q. Zhao, J. Jiang and L. Wei, *Chem. Eng. J.*, 2023, **477**, 146867.
37 Y. Zhong, J.-Q. Chang, C.-H. Hu and J. Zhou, *J. Mol. Struct.*, 2020, **1222**, 128938.
38 H. Zhang, M. Lü, S. Liu, L. Wang, Z. Xiu, Y. Zhou, Z. Qiu, A. Zhang and Q. Ma, *Mater. Chem. Phys.*, 2009, **114**, 716–721.
39 J. Y. Chen, J. J. Lu, X. G. Tang, W. M. Zhong, R. Li, Q. J. Sun, Y. P. Jiang, W. H. Li and Q. X. Liu, *Vacuum*, 2024, **226**, 113321.
40 D. A. Solís-Casados, L. Escobar-Alarcón, V. Alvarado-Pérez and E. Haro-Poniatowski, *Int. J. Photoenergy*, 2018, **2018**, 1–9.
41 M.-C. Wu, Y.-H. Chang and T.-H. Lin, *Jpn. J. Appl. Phys.*, 2017, **56**, 04CJ01.

42 P. Li, C. Jiang, Q. Wang, K. Zuojiao, Z. Zhang, J. Liu and Y. Wang, *J. Nanosci. Nanotechnol.*, 2018, **18**, 8360–8366.
43 K. V. Pham, V. H. Nguyen, D. P. Nguyen, D. B. Do, M. O. Le and H. H. Luc, *J. Electron. Mater.*, 2017, **46**, 6829–6833.
44 N. Thanabodeekij, E. Gulari and S. Wongkasemjit, *Powder Technol.*, 2005, **160**, 203–208.
45 Z. Bian, Y. Huo, Y. Zhang, J. Zhu, Y. Lu and H. Li, *Appl. Catal., B*, 2009, **91**, 247–253.
46 H. X. Liu, H. Mei, N. X. Miao, L. K. Pan, Z. P. Jin, G. Q. Zhu, J. Z. Gao, J. J. Wang and L. F. Cheng, *Chem. Eng. J.*, 2021, **414**, 128748.
47 H. Shi, J. Fu, W. Jiang, Y. Wang, B. Liu, J. Liu, H. Ji, W. Wang and Z. Chen, *Colloids Surf., A*, 2021, **615**, 126063.
48 N. Li, M. Shi, Y. Xin, W. Zhang, J. Qin, K. Zhang, H. Lv, M. Yuan and C. Wang, *J. Environ. Chem. Eng.*, 2022, **10**, 107420.
49 J. Chen, W. G. Mei, C. Liu, C. H. Hu, Q. J. Huang, N. N. Chen, J. Chen, R. Zhang and W. H. Hou, *Mater. Lett.*, 2016, **172**, 184–187.
50 S. Xu, W. Shangguan, J. Yuan, J. Shi and M. Chen, *Mater. Sci. Eng., B*, 2007, **137**, 108–111.
51 H. He, J. Yin, Y. Li, Y. Zhang, H. Qiu, J. Xu, T. Xu and C. Wang, *Appl. Catal., B*, 2014, **156–157**, 35–43.
52 J. Wang, W. W. Liu, D. L. Zhong, Y. J. Ma, Q. Y. Ma, Z. Y. Wang and J. Pan, *J. Mater. Sci.*, 2019, **54**, 13740–13752.
53 H. Gan, J. Liu, H. Zhang, Y. Qian, H. Jin and K. Zhang, *Res. Chem. Intermed.*, 2017, **44**, 2123–2138.
54 Y. Bespalko, N. Eremeev, E. Sadovskaya, T. Krieger, O. Bulavchenko, E. Suprun, M. Mikhailenko, M. Korobeynikov and V. Sadykov, *Membranes*, 2023, **13**, 598.
55 K. Qian, L. Xia, W. Wei, L. Chen, Z. Jiang, J. Jing and J. Xie, *Mater. Lett.*, 2017, **206**, 245–248.
56 H. Dislich, *Angew. Chem., Int. Ed. Engl.*, 1971, **10**, 363–370.
57 Z. Chen, H. Jiang, W. Jin and C. Shi, *Appl. Catal., B*, 2016, **180**, 698–706.
58 C.-L. Zhang and S.-H. Yu, *Chem. Soc. Rev.*, 2014, **43**, 4423–4448.
59 D. X. Ji, Y. G. Lin, X. Y. Guo, B. Ramasubramanian, R. W. Wang, N. Radacsi, R. Jose, X. H. Qin and S. Ramakrishna, *Nat. Rev. Methods Primers*, 2024, **4**, 2.
60 D. Hou, W. Luo, Y. Huang, J. C. Yu and X. Hu, *Nanoscale*, 2013, **5**, 2028–2035.
61 M. C. M. D. de Conti, S. Dey, W. E. Pottker and F. A. La Porta, *Mater. Today Sustainability*, 2023, **23**, 100458.
62 S. Niu, R. Zhang, Z. Zhang, J. Zheng, Y. Jiao and C. Guo, *Inorg. Chem. Front.*, 2019, **6**, 791–798.
63 W. Li, Y. Zuo, L. Jiang, D. Yao, Z. Chen, G. He and H. Chen, *Mater. Chem. Phys.*, 2020, **256**, 123250.
64 X. Ren, Y. Chu, S. Yuan, Y. Zheng, Z. Zeng, C. Xia, L. Zhao, Y. Wu and Y. He, *J. Environ. Manage.*, 2024, **370**, 122776.
65 W. Liu, C. Wei, R. Peng, R. Chu, H. Sun, X. Zhang and F. Xie, *New J. Chem.*, 2022, **46**, 10854–10862.
66 P. Li, C. Jiang, C. Feng and Y. Wang, *Mater. Chem. Phys.*, 2020, **252**, 123650.
67 V. Jayaraman, C. Ayappan, G. Vattikondala and A. Mani, *Mater. Res. Bull.*, 2021, **143**, 111439.
68 Z. Zhang, C. Jiang, P. Du and Y. Wang, *Ceram. Int.*, 2015, **41**, 3932–3939.
69 G. F. Samu, Á. Veres, B. Endrődi, E. Varga, K. Rajeshwar and C. Janáky, *Appl. Catal., B*, 2017, **208**, 148–160.
70 Y. Liu, G. Zhu, J. Peng, J. Gao, C. Wang and P. Liu, *J. Mater. Sci.: Mater. Electron.*, 2016, **28**, 2172–2182.
71 L. Jinhai, M. Han, Y. Guo, F. Wang, L. Meng, D. Mao, S. Ding and C. Sun, *Appl. Catal., A*, 2016, **524**, 105–114.
72 S. Gupta, L. De Leon and V. R. Subramanian, *Phys. Chem. Chem. Phys.*, 2014, **16**, 12719–12727.
73 B. Allured, S. DelaCruz, T. Darling, M. N. Huda and V. Subramanian, *Appl. Catal., B*, 2014, **144**, 261–268.
74 H. Tian, K. Chen, X. Ye, S. Yang and Q. Gu, *Ceram. Int.*, 2019, **45**, 20750–20757.
75 H. Liu, Y. Chen, G. Tian, Z. Ren, C. Tian and H. Fu, *Langmuir*, 2015, **31**, 5962–5969.
76 Y. Xu, D. Lin, X. Liu, Y. Luo, H. Xue, B. Huang, Q. Chen and Q. Qian, *ChemCatChem*, 2018, **10**, 2496–2504.
77 Y. Zhao, H. Fan, K. Fu, L. Ma, M. Li and J. Fang, *Int. J. Hydrogen Energy*, 2016, **41**, 16913–16926.
78 D. Liu, J. Zhang, C. Li, X. Zhang, X. Chen, F. Wang, M. Shi, R. Li and C. Li, *Appl. Catal., B*, 2019, **248**, 459–465.
79 Y. Du, Q. Hao, D. Chen, T. Chen, S. Hao, J. Yang, H. Ding, W. Yao and J. Song, *Catal. Today*, 2017, **297**, 255–263.
80 J. G. Hou, S. Q. Jiao, H. M. Zhu and R. V. Kumar, *J. Solid State Chem.*, 2011, **184**, 154–158.
81 A. G. Krasnov, M. S. Koroleva, M. I. Vlasov, I. R. Shein, I. V. Piir and D. G. Kellerman, *Inorg. Chem.*, 2019, **58**, 9904–9915.
82 C. L. Mayfield and M. N. Huda, *J. Cryst. Growth*, 2016, **444**, 46–54.
83 A. Phuruangrat, S. Buapoon, T. Bunluesak, P. Suebsom, S. Wannapop, T. Thongtem and S. Thongtem, *J. Aust. Ceram. Soc.*, 2022, **58**, 999–1008.
84 Z. Khazaee, A. H. C. Khavar, A. R. Mahjoub, A. Motaee, V. Srivastava and M. Sillanpää, *Sol. Energy*, 2020, **196**, 567–581.
85 R. Tai, R. Wu, M. Zhang, J. Yuan, J. Tressel, Y. Tang, Q. Wang and S. Chen, *Curr. Opin. Chem. Eng.*, 2024, **45**, 101033.
86 X. Ding, X. Xu, J. Wang, Y. Xue, J. Wang, Y. Qin and J. Tian, *J. Colloid Interface Sci.*, 2024, **662**, 727–737.
87 N. Li, Y. Niu, W. An, Z. Liu, F. Ruan and G. Fan, *J. Colloid Interface Sci.*, 2024, **669**, 175–189.
88 N. Li, J. Wu, H.-B. Fang, X.-H. Zhang, Y.-Z. Zheng and X. Tao, *Appl. Surf. Sci.*, 2018, **448**, 41–49.
89 W. H. Glaze, J. W. Kang and D. H. Chapin, *Ozone: Sci. Eng.*, 1987, **9**, 335–352.
90 Y. Ou, J. Shi, Q. Yan, C. Li and Y. Zheng, *Inorg. Chem. Commun.*, 2021, **133**, 108867.
91 L. Jie, X. Gao, X. Cao, S. Wu, X. Long, Q. Ma and J. Su, *Mater. Sci. Semicond. Process.*, 2024, **176**, 108288.
92 V. Jayaraman, C. Ayappan, G. Vattikondala and A. Mani, *Mater. Res. Bull.*, 2021, **143**, 111439.
93 R. J. Walker, A. Pougin, F. E. Oropeza, I. J. Villar-Garcia, M. P. Ryan, J. Strunk and D. J. Payne, *Chem. Mater.*, 2015, **28**, 90–96.
94 P. Li, R. Wu, P. Li, S. Gao, Z. Qin, X. Song, W. Sun, Z. Hua, Q. Wang and S. Chen, *Adv. Sci.*, 2024, **11**, e2408829.
95 Y. Gao, Z. Zhan, L. Guo, Z. Li, S. Cai, X. Wang, M. Li, Y. Xie and W. Zhou, *Small*, 2025, **21**, e2410883.